Multi-Resonant Metamaterial Absorber for Electromagnetic Absorption in S-, C-, X-, and Ku- Band

Iftikhar Ud Din * , Daud Khan , Sarosh Ahmad , Tayeb A. Denidni

Posted Date: 27 April 2026

doi: 10.20944/preprints202604.1889.v1

Keywords: absorber; resonator; hybrid structure; surface impedance; free space

 doi:10.20944/preprints202604.1889.v1

Article

Multi-Resonant Metamaterial Absorber for Electromagnetic Absorption in S-, C-, X-, and Ku- Band

Iftikhar Ud Din *, Daud Khan, Sarosh Ahmad and Tayeb A. Denidni

National Institute for Scientific Research (INRS), University du Quebec, Montreal, QC H5A 1K6, Canada
* Correspondence: iftikhar.ud-din@inrs.ca

Abstract

This work introduces a compact multi-resonant metamaterial absorber designed to achieve efficient electromagnetic absorption over several microwave frequency bands. The proposed configuration is based on a hybrid resonator arrangement that promotes strong electromagnetic interaction and enables multiple resonant modes within a single unit cell. Consequently, six distinct absorption peaks are obtained at 2.4, 5.21, 6.88, 9.77, 12.61, and 14.99 GHz, covering S-, C-, X-, and Ku-band applications. The absorber exhibits high absorption performance, exceeding 97% across most operating frequencies, which indicates effective impedance matching with free space and efficient energy dissipation mechanisms. The absorption characteristics are further examined through surface current distributions, electric field confinement, and effective medium analysis, demonstrating that the multi-band response originates from the interaction of multiple resonant elements and intrinsic material losses. Moreover, the proposed structure maintains stable performance for different polarization angles and oblique wave incidence, confirming its polarization-insensitive and angularly stable behavior. To validate the design, a prototype is fabricated and experimentally characterized using a free-space measurement setup, showing close agreement with the simulated results. The compact geometry, low fabrication cost, and scalability of the proposed absorber make it a promising candidate for applications such as electromagnetic interference mitigation, radar cross-section reduction, and modern wireless communication systems.

Keywords: metamaterial; absorber; resonator; hybrid structure; surface impedance; free space

1. Introduction

The rapid growth of wireless communication systems, radar technologies, and compact electronic devices has resulted in a substantial increase in electromagnetic (EM) radiation across the microwave frequency spectrum [1,2]. Contemporary technologies such as Wi-Fi, sub-6 GHz and millimeter-wave (mmWave) 5G networks, satellite communication systems, Internet of Things (IoT) devices, and advanced sensing platforms operate concurrently over multiple frequency bands. This spectral congestion leads to severe electromagnetic as well as radio-frequency interference effects, signal distortion, and overall system performance degradation [3,4]. Consequently, the development of efficient electromagnetic absorbers capable of suppressing unwanted reflections and mitigating interference has become a critical research challenge [5]. Conventional microwave absorbers, including Salisbury screens, Jaumann absorbers, and Dallenbach layers, typically employ resistive sheets combined with quarter-wavelength spacing to achieve absorption at specific frequencies [6,7]. While these structures provide reasonable absorption performance, they inherently suffer from large physical thickness, narrow operating bandwidth, and limited tunability, particularly at lower microwave frequencies [8]. Such drawbacks significantly restrict their integration into modern compact, lightweight, and multi-functional electronic systems required for advanced wireless and stealth applications [9]. Metamaterial absorbers (MMAs) have emerged as a compelling instead of traditional absorbers as a result of their ability to manipulate electromagnetic waves using artificially engineered subwavelength resonant

 doi:10.20944/preprints202604.1889.v1

elements rather than relying solely on bulk material properties [10,11]. Since the demonstration of a close-to-unity metamaterial absorber utilizing on impedance-matching principles by Landy *et al*, MMAs have attracted considerable research interest across microwave, terahertz, infrared, and optical frequency regimes [12,13]. By simultaneously tailoring the effective electric permittivity and magnetic permeability, MMAs can significantly suppress both reflection and transmission, thereby enabling near-unity absorption within electrically thin and compact structures [14].Typically, metamaterial absorbers are realized through a three-layer arrangement consisting of a structured metallic surface, a dielectric spacer, and a conductive ground layer [15]. The ground plane effectively blocks electromagnetic transmission, while the interaction between the resonant top layer and the dielectric substrate facilitates impedance matching with free space. As a result, incident electromagnetic energy is efficiently dissipated through dielectric and ohmic losses [16,17]. By tuning the resonator geometry, substrate characteristics, and electromagnetic coupling mechanisms, MMAs are capable of operating over desired frequencies with high absorption efficiency [18]. Based on their spectral response, metamaterial absorbers are generally classified into single-band, multiband, and broadband categories [19]. Single-band absorbers offer high frequency selectivity and are widely employed in sensing and narrowband EMI suppression applications [20]. However, the growing demand for multifunctional and multi-standard wireless systems has shifted research interest toward multiband and broadband absorbers capable of operating over multiple discrete or continuous frequency ranges [21]. Multiband metamaterial absorbers provide an effective solution for addressing several wireless standards simultaneously without increasing structural complexity or device footprint [22]. Numerous multiband metamaterial absorbers have been reported using nested resonators, hybrid geometries, and coupled resonant elements [23,24]. Dual- and triple-band absorbers targeting Wi-Fi, sub-6 GHz 5G, and X-band radar applications have demonstrated absorption levels exceeding 90% at selected frequencies [25,26]. Nevertheless, many existing designs remain limited by a small number of resonant bands, reduced absorption efficiency at higher frequencies, or inadequate scalability across widely separated microwave bands [27]. Although recent studies have explored absorbers operating in the Ku-band and higher microwave frequencies for radar stealth, satellite communications, and EMI shielding [28,29], achieving stable multiband absorption that simultaneously covers lower microwave bands bands centered around 2.4 GHz and spanning 5–7 GHz remains challenging due to increased electrical size and impedance mismatch issues [30]. Therefore, compact multiband metamaterial absorbers capable of delivering high absorption efficiency across both lower and upper microwave bands are still highly desirable [31].

This study presents a microwave metamaterial absorber with a compact and efficient multi-resonant design, exhibiting multiple well-defined absorption bands with peaks at 2.4 GHz, 5.21 GHz, 6.88 GHz, 9.77 GHz, 12.61 GHz, and 14.99 GHz, thereby covering several widely used wireless communication and radar frequency bands. At these operating frequencies, the absorber achieves absorption efficiencies exceeding 97%, with peak absorptivity values of approximately 98.23%, 97.98%, 98.23%, 97.73%, 91.13%, and 97.43%, respectively. This performance favorably compares with and, in many cases, surpasses previously reported multiband absorbers in terms of both absorption magnitude and spectral coverage [32]. The observed multiband absorption behavior arises due to the presence of multiple resonant modes in the optimized unit cell, ensuring improved impedance matching with free space at each resonance frequency [33,34]. This mechanism minimizes reflection and ensures near-zero transmission, resulting in efficient dissipation of incident electromagnetic energy [35]. Owing to its compact size, planar configuration, and high absorption efficiency across multiple microwave bands, the absorber is well suited for applications like EMI control, protection of wireless communication systems, and reduction of radar visibility, and multiband microwave systems [36,37].

The remainder of this paper is organized as follows. Section 2 presents the electromagnetic excitation mechanism and the optimization of the proposed layered metamaterial absorber architecture. Section 3 details the design configuration, numerical modeling, and optimization procedure used to achieve the desired absorption performance. Section 4 explains the fundamental absorption mechanism

 doi:10.20944/preprints202604.1889.v1

responsible for the observed resonant behavior. Section 5 investigates the polarization-dependent absorption response of the proposed structure, while Section 6 analyzes its angular stability under oblique incidence for different polarization modes. Section 7 examines the distributions of surface currents and electric fields to provide physical insight into the resonance formation and energy dissipation mechanisms. Section 8 discusses the frequency-dependent effective electromagnetic parameters of the absorber, including permittivity, permeability, and normalized impedance. Section 9 presents the experimental validation through measured absorption results, followed by Section 10, which provides a comparative analysis with previously reported designs. Finally, Section 11 concludes the paper by summarizing the key findings and main contributions of the proposed metamaterial absorber.

2. Electromagnetic Excitation Mechanism and Optimization of the Layered Architecture

Figure 1 illustrates the electromagnetic configuration and Absorption Profile of the multiband Artificial EM absorber operating in the microwave frequency spectrum. The structure exhibits multiple distinct absorption resonances within the GHz spectrum, with pronounced absorption peaks occurring at 2.4 GHz, 5.21 GHz, 6.88 GHz, 9.77 GHz, 12.61 GHz, and 14.99 GHz, respectively. At these frequencies, the absorber achieves high absorption efficiency exceeding 97%, with peak absorptivity values of approximately 98.23%, 97.98%, 98.23%, 97.73%, 91.13%, and 97.43%, respectively. These results confirm that the proposed metasurface supports multiple distinct resonant modes, each responsible for efficient electromagnetic energy dissipation at its corresponding resonance frequency.Unlike terahertz absorbers that typically require optical or spectroscopic characterization techniques, the proposed design operates in the microwave domain. As a result, its experimental validation can be conveniently performed using vector network analyzer (VNA) based free-space measurement setups. The absorber is composed of a metasurface unit cell formed by a patterned metallic resonator developed on an FR-4 dielectric layer. The resonator geometry follows a concentric hybrid configuration that combines square, circular, dodecagonal, and diamond-shaped elements. Intense electromagnetic interaction among the resonators gives rise to multiple resonances, contributing to stable performance multiband absorption across the 1-16 GHz frequency range. At each operating band, the metasurface achieves effective impedance matching with free space, which significantly suppresses reflection while maintaining minimized transmission beacause of metallic ground layer. Consequently, near-perfect absorption is obtained at distinct resonance frequency points. As depicted in Figure 1, the absorber is excited by an incident electromagnetic wave can be represented by the electromagnetic wave is represented by the electric field (E), magnetic field (H), and propagation vector (k), which are defined according to the selected incidence angle (θ) and polarization angle (ϕ). These excitation conditions are essential for evaluating the angular stability, polarization insensitivity, and resonance robustness of the absorber under realistic operating scenarios. Furthermore, strong localization of the electromagnetic fields within the metasurface at resonance enhances both dielectric and conductive losses within the lossy substrate, directly contributing to the observed high absorption levels. The ability of the proposed design to maintain consistently high absorptivity across multiple discrete microwave bands highlights its effectiveness and confirms its suitability for real-world applications including electromagnetic interference mitigation, reduction of radar cross-section, and microwave stealth technologies.

 doi:10.20944/preprints202604.1889.v1

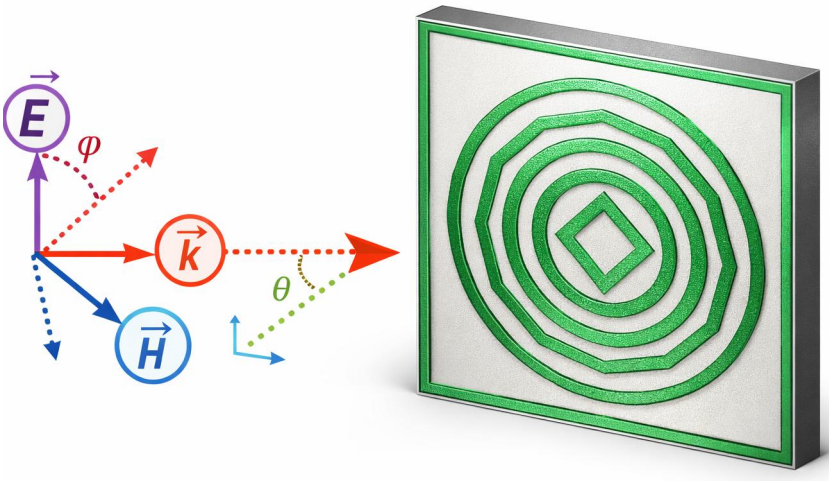

Figure 1. illustrating how an incident electromagnetic wave interacts with the proposed multilayer absorber, highlighting the orientations of the electric field, magnetic field, and propagation direction relative to the structure.

3. Design Configuration, Simulation and Optimization

The unit cell configuration of the developed metamaterial absorber is presented in Figure 2, where the front and backside layouts are shown in Figure 2(a,b), respectively. The structure is composed of three distinct layers, including a patterned conductive layer on the top, a dielectric medium in the middle, and a solid metallic layer at the bottom. The bottom metallic sheet is implemented using copper and acts as a reflector, preventing the transmission of incident electromagnetic waves. This ensures that the transmission coefficient remains negligible, which is a fundamental requirement for maximizing absorption performance. The top layer consists of a copper-based resonating pattern with a conductivity of 5.8×10^7 S/m and a thickness of 0.035 mm. This layer is responsible for inducing strong localized currents, which contribute to resonant energy confinement with reduced resistive losses. An FR-4 substrate is used as the intermediate layer, characterized by a relative permittivity of $\varepsilon_r = 4.4$ and a thickness of 1.6 mm. This dielectric spacing plays an essential role in regulating the interaction between the resonator and the ground plane, enabling proper impedance matching with free space. The structural dimensions were adjusted through a detailed parametric analysis to generate multiple resonant modes associated with both electric and magnetic responses. This design strategy leads to the realization of multi-band absorption behavior. The final optimized values of the design variables are provided in Table 1.

Table 1. Design variables of the Developed Model Metamaterial Absorber.

Design variables	Size (mm)	Design variables	Size (mm)
w_s	13	l_s	13
w_g	13	l_g	13
w_p	12.75	l_p	12.75
R	5.5	R_1	4.5
R_2	3.5	R_3	2.5
s_q	2.5	h_c	0.035

 doi:10.20944/preprints202604.1889.v1

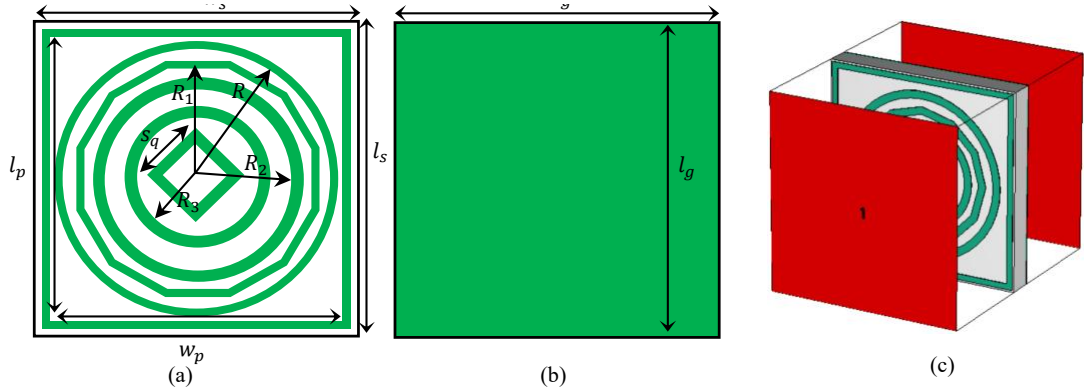

Figure 2. Configuration of the proposed MMA absorber.

Figure 3 show Full-wave electromagnetic simulations were performed by modeling an one unit cell under periodic conditions applied at the boundaries along the in the transverse (x–y) directions, thereby emulating an infinite two-dimensional metasurface array. Open (radiation) boundary conditions were introduced along the z-direction to accurately represent open-space wave propagation. The absorber was excited using a normally incident plane wave over the frequency range of 1-16 GHz, corresponding to the intended operational frequency range of the MMA. All numerical analyses were executed using the frequency-domain solver available in CST Microwave Studio ensure accurate characterization of the steady-state electromagnetic response of the absorber. Floquet ports were employed to excite the structure, preserving the periodic nature of the incident wavefront and enabling precise extraction of the scattering parameters, while also allowing for the analysis of oblique incidence. To ensure numerical accuracy, a finite-element-based discretizations scheme was adopted, with adaptive mesh refinement applied in regions exhibiting strong electromagnetic field variations. This meshing strategy provides an optimal trade-off between computational efficiency and accuracy. The frequency-dependent scattering parameters obtained from the simulations were subsequently used to evaluate the absorption coefficient of the proposed structure. The absorption performance of the presented metamaterial structure is evaluated using the well-known expression

$$A = 1 - |S_{11}|^2 - |S_{21}|^2 \tag{1}$$

In this expression, $|S_{11}|^2$ corresponds to the reflected power ratio, while $|S_{21}|^2$ denotes the transmitted power ratio through the structure. For the proposed absorber, a continuous metallic ground layer is incorporated at the bottom, which effectively blocks wave transmission. Consequently, the transmission term becomes negligible, i.e., $|S_{21}|^2 \approx 0$. Under this condition, the absorption expression can be reduced to

$$A = 1 - |S_{11}|^2 \tag{2}$$

indicating the absorption performance is controlled by reflection minimization. The proposed structure exhibits multiple resonant absorption modes across the microwave frequency spectrum. Distinct absorption peaks are observed at 2.4 GHz, 5.21 GHz, 6.88 GHz, 9.77 GHz, 12.61 GHz, and 14.99 GHz. At these frequencies, the absorber demonstrates strong absorption performance exceeding 97%, with peak absorptivity values of approximately 98.23%, 97.98%, 98.23%, 97.73%, 91.13%, and 97.43%, respectively. These results confirm that the metasurface supports multiple electromagnetic resonances originating from different current paths and LC coupling mechanisms within the unit cell.

 doi:10.20944/preprints202604.1889.v1

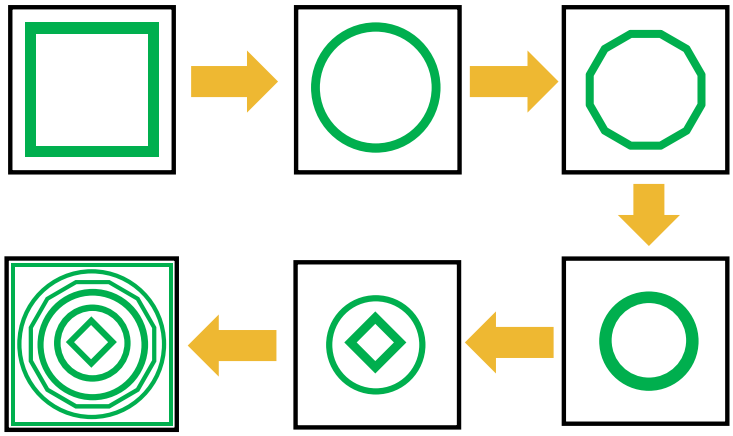

Figure 3. Design steps of the presented Absorber.

Figure 4 illustrates the progressive optimization of the Geometric layout of the unit cell, while the corresponding absorption response at each design stage is presented to elucidate the contribution of individual resonant features. In Step 1, the initial configuration exhibits a strong absorption resonance at 2.4 GHz with a near-unity absorptivity of 0.99, indicating effective impedance matching in the lower microwave band. With the introduction of additional structural elements in Step 2, a new resonance appears at 4.9 GHz, achieving an absorption level of approximately 0.80. Further geometric refinement in Step 3 shifts the resonance to 6.49 GHz, where a comparable absorptivity of 0.80 is maintained, demonstrating stable mid-band absorption behavior. In Step 4, the structure supports maximum absorption observed at 9 GHz with a moderate absorptivity of 0.60. Subsequently, Step 5 introduces an additional resonance at 12 GHz with an improved absorption level of 0.76. These intermediate stages clearly illustrate how successive geometric modifications activate new resonant modes and progressively expand the operational bandwidth. Based on this systematic design evolution, the final optimized layout exhibits multiple well-defined absorption resonances across the microwave spectrum as depicted in Figure 4. This multi-resonant absorption response confirms that the final configuration effectively integrates the individual resonant contributions identified during the design stages, resulting in enhanced absorption strength and wide spectral coverage suitable for practical microwave applications.

 doi:10.20944/preprints202604.1889.v1

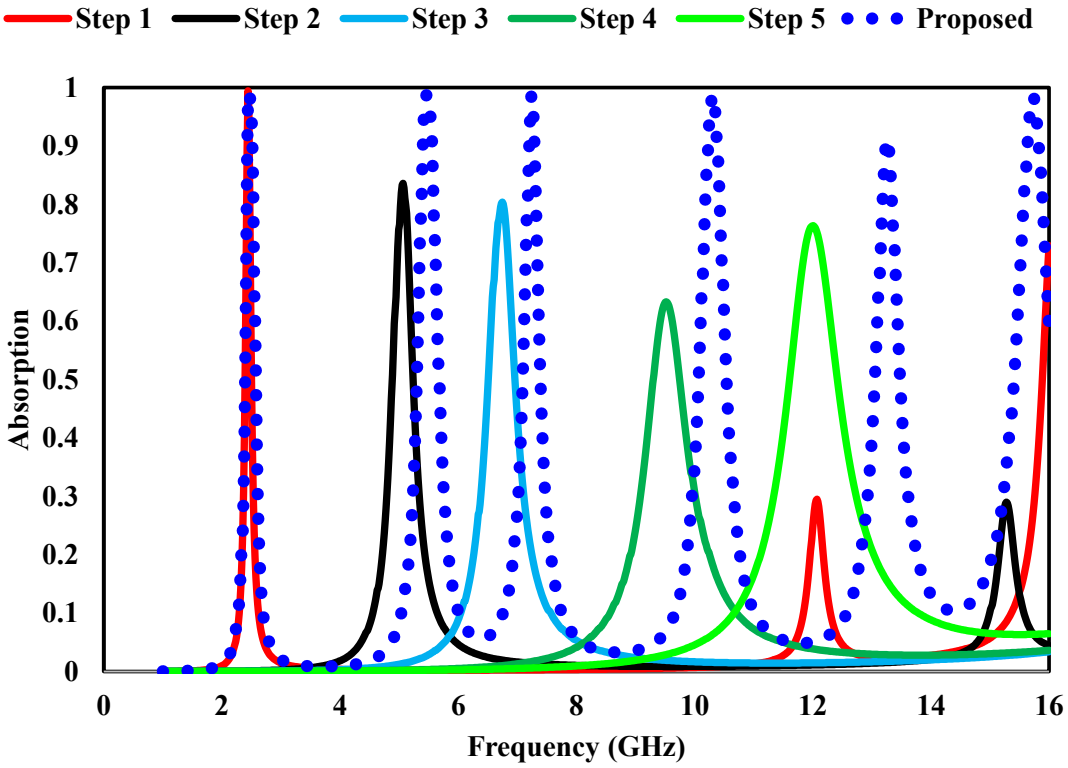

Figure 4. Simulated response of the proposed optimization steps.

4. Absorption Mechanism

Figure 5 presents the simulated scattering parameters together with the corresponding absorption behavior of the proposed unit cell. The results include the response under both transverse electric (TE) and transverse magnetic (TM) excitations. The absorption profile, derived from the S-parameters, indicates the presence of several distinct resonant peaks distributed over the microwave frequency spectrum. Significant absorption levels are achieved at approximately 2.4 GHz, 5.21 GHz, 6.88 GHz, 9.77 GHz, 12.61 GHz, and 14.99 GHz, where the absorptivity remains above 97% for most of these resonances. At these frequencies, the structure approaches near-complete absorption, which suggests effective impedance matching between the metasurface and free space. In metamaterial absorbers, such behavior is typically obtained when both reflection and transmission are minimized. Furthermore, the responses obtained under TE and TM polarizations closely overlap, demonstrating that the design maintains polarization-insensitive performance. The combination of copper layers and the FR-4 dielectric substrate contributes to consistent absorption efficiency across the operating bands. Overall, the unit cell exhibits multiple resonant absorption peaks over a wide frequency range, indicating its suitability for broadband microwave applications where stable and polarization-independent absorption is required.

 doi:10.20944/preprints202604.1889.v1

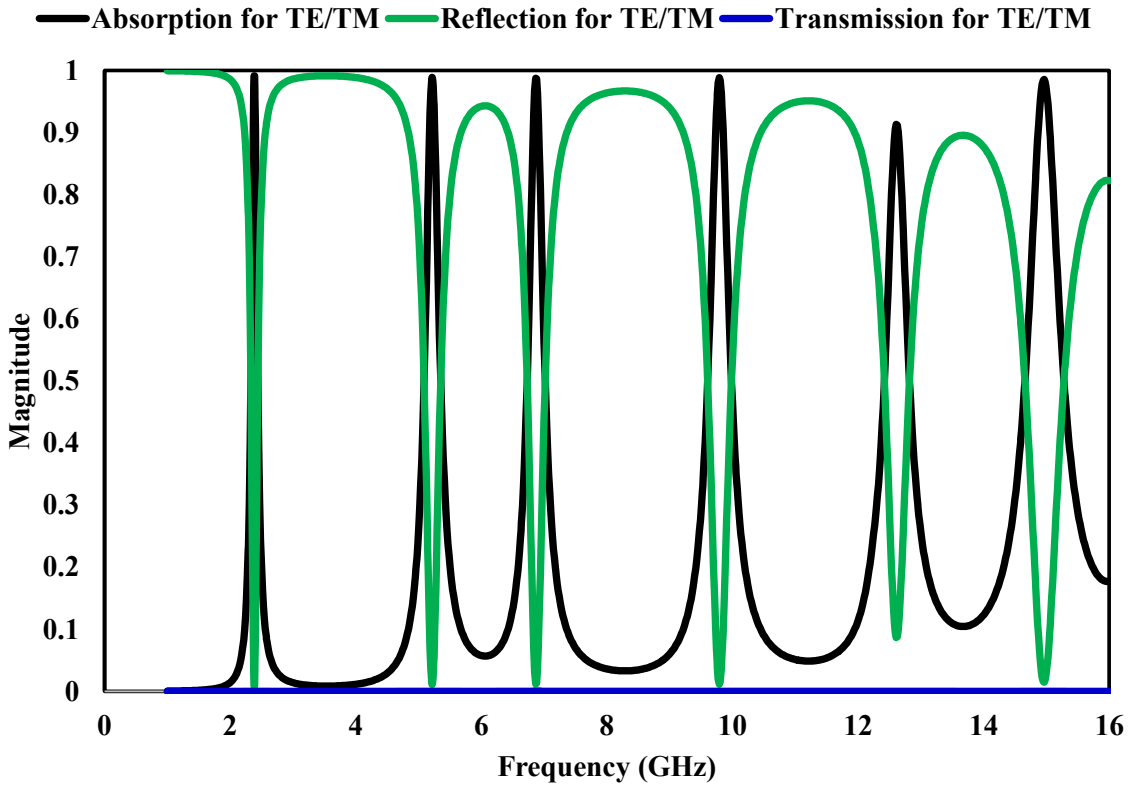

Figure 5. Absorption spectra evaluated for electromagnetic waves with both TE and TM polarization states when incident normally on the structure.

5. Polarization-Independent Absorption Response

Polarization independence and angular robustness are critical indicators when evaluating the performance of electromagnetic absorbers. A well-designed absorber exhibit consistent absorption regardless of the orientation of the incident electric field. Figure 6 illustrates the simulated absorption response of the proposed structure for various polarization angles ($\phi = 15°, 30°, 45°, 60°, 75°$, and $90°$) under normal incidence. The obtained results show that the absorption peaks remain nearly unaffected across all polarization states, demonstrating that the structure operates independently of po This behavior is attributed to the symmetric configuration of the unit cell. Structures with rotational symmetry are known to provide identical electromagnetic responses for different polarization orientations. In the present design, the fourfold symmetry ensures uniform interaction with the incident wave along both orthogonal directions. As a result, the absorber preserves stable absorption characteristics over a wide range of polarization angles.

 doi:10.20944/preprints202604.1889.v1

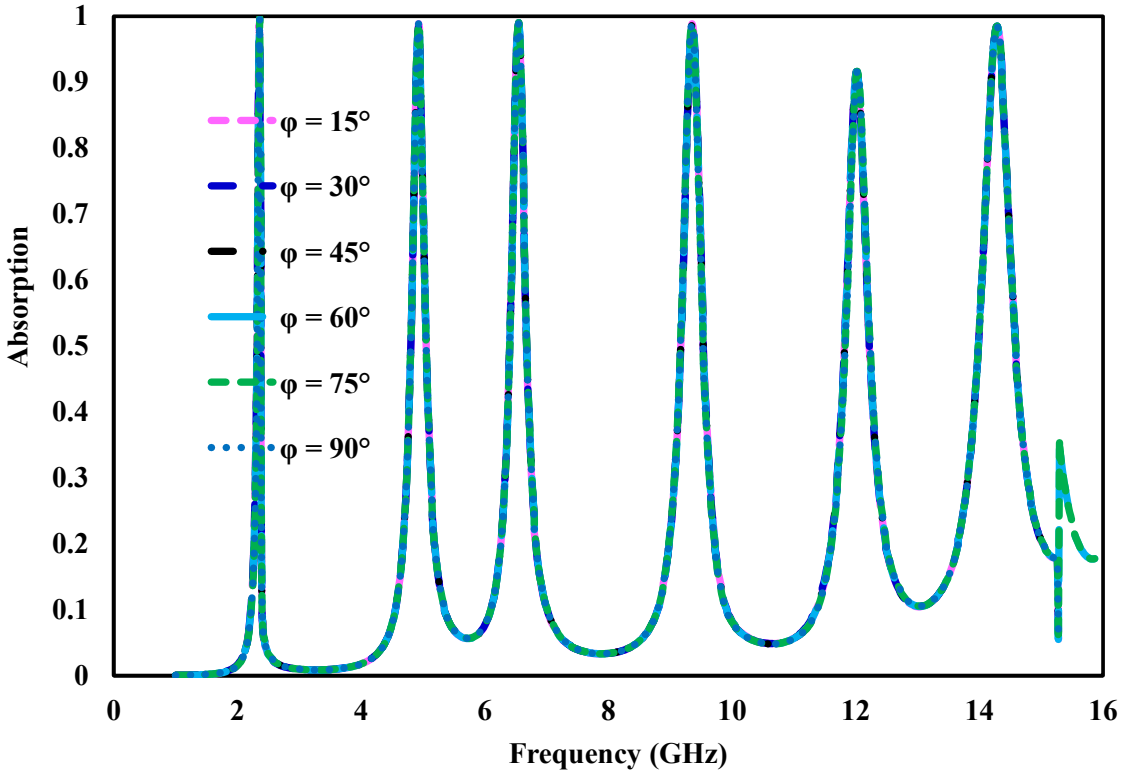

Figure 6. Simulated absorptivity response of the proposed metamaterial absorber for different polarization angles.

6. Angular-Dependent Absorption Characteristics

In practical electromagnetic environments, incident waves may arrive from different directions rather than only normal incidence. To examine this behavior, the response of the proposed multi-band absorber was investigated under oblique incidence conditions for both transverse electric (TE) and transverse magnetic (TM) polarizations. Figure 7 presents the simulated absorption results for incidence angles of $\theta = 0^\circ, 15^\circ, 30^\circ$, and 45° for both polarization modes. It can be observed that the absorber maintains strong absorption performance, with values remaining above 85% across the considered angular range. Such behavior indicates a high level of angular stability, which is an important requirement for practical absorber applications. As the incident angle increases, a slight reduction in absorption efficiency is noticeable. In particular, minor variations in the absorption spectrum appear at higher frequencies. This effect is mainly attributed to changes in the distribution of the electromagnetic fields and the resulting coupling between resonant elements, which becomes more pronounced at oblique incidence angles, where variations in field components lead to impedance mismatch at larger angles. Despite these variations, the absorber continues to demonstrate reliable performance over a wide range of incidence angles for both TE and TM polarizations. This confirms its suitability for real-world microwave and radar systems, where the direction of incoming waves cannot be controlled.

 doi:10.20944/preprints202604.1889.v1

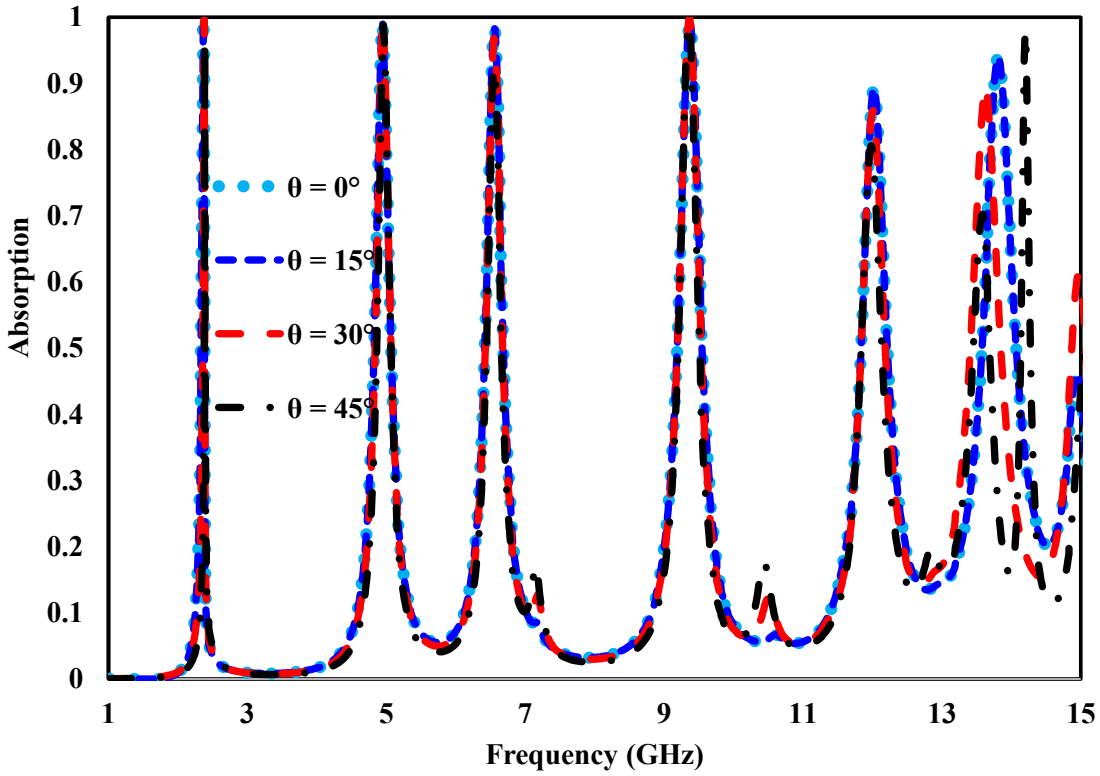

Figure 7. Simulated absorptivity response of the proposed metamaterial absorber under different incidence angles (θ).

7. Surface Currents and Electric Field Distributions

Figure 8(a–f) illustrate the the current flow pattern across the resonator surface on the absorber at 2.38, 5.2, 6.8, 9.7, 12.6, and 14.96 GHz, respectively, where the arrow density and color intensity indicate the magnitude and direction of the induced currents. At 2.38 GHz, strong Surface charge flow are predominantly confined along the outermost square ring and the inter-cell metallic boundaries, forming large closed current loops. This confirms showing that the primary resonant mode appears at the lowest frequency band is mainly dependent on the outer resonator and Inter-element coupling. As the frequency shifts upward to 5.2 GHz, the current density shifts inward and becomes primarily localized on the outer circular ring, while the outer square ring exhibits weaker excitation, indicating a transition of the dominant resonant path. At 6.8 GHz, the surface currents are strongly confined to the middle circular ring, with symmetric circulating currents clearly visible around its circumference, demonstrating that the ring contributes to the the corresponding absorption band. At 9.7 GHz, the current distribution further contracts toward the inner circular ring, where dense and well-defined current loops are observed, confirming the excitation of a higher-order resonant mode. At 12.6 GHz, intense currents are concentrated mainly around the central diamond-shaped resonator, while the surrounding rings show relatively reduced current levels, indicating that the innermost metallic structure dominates this resonance. Finally, at 14.96 GHz, strong surface currents are simultaneously observed on the central diamond and the adjacent inner circular ring, revealing pronounced electromagnetic coupling between closely spaced resonators at the highest operating frequency. Across all frequencies, the current distributions exhibit clear symmetry within each unit cell, confirming stable resonance behavior and demonstrating that the multi-band absorption arises from a progressive inward activation of resonant elements, with mutual coupling enhancing the overall absorption performance. Figure 9(a–f) also illustrate the Electromagnetic field component magnitude variation of the proposed absorber at the same operating resonant bands, where the color scale from blue to red represents increasing electric-field . At 2.38 GHz, the Electromagnetic field component is

 doi:10.20944/preprints202604.1889.v1

strongly concentrated along the outer boundaries of the square unit cell and the outermost circular ring, with pronounced field enhancement near the square frame edges.This indicates dominant capacitive coupling between the incident wave and the outer resonator, corresponding to the lowest-frequency resonance. At 5.2 GHz, the high-intensity electric field shifts inward and becomes mainly localized on the outer circular ring, while the square boundary shows reduced excitation, confirming that the circular resonator governs this absorption band. At 6.8 GHz, the electric field is further confined toward the middle circular ring, forming a well-defined high-field region around its circumference, which demonstrates excitation of an intermediate electric resonance with limited involvement of the outer structures. At 9.7 GHz, the electric-field distribution becomes more compact and is primarily concentrated on the inner circular ring, with strong field accumulation visible along the upper and lower portions of the ring structure, indicating excitation of a higher-order localized electric mode. At 12.6 GHz, intense electric-field improvement is clearly identified around the central diamond-shaped resonator, while the surrounding circular rings exhibit comparatively weaker field intensities, confirming that the innermost metallic element dominates this resonance through strong capacitive effects. Finally, at 14.96 GHz, strong electric-field regions appear simultaneously around the central diamond and the adjacent inner circular ring, accompanied by noticeable field intensification at the inter-cell junctions, revealing strong electromagnetic coupling between closely spaced resonators at the highest operating frequency. Overall, the electric-field distributions demonstrate a progressive inward shift of field localization with increasing frequency, confirming that each absorption band is associated with a distinct resonant element and that mutual coupling between resonators contributes to the broadband multiband absorption behavior.

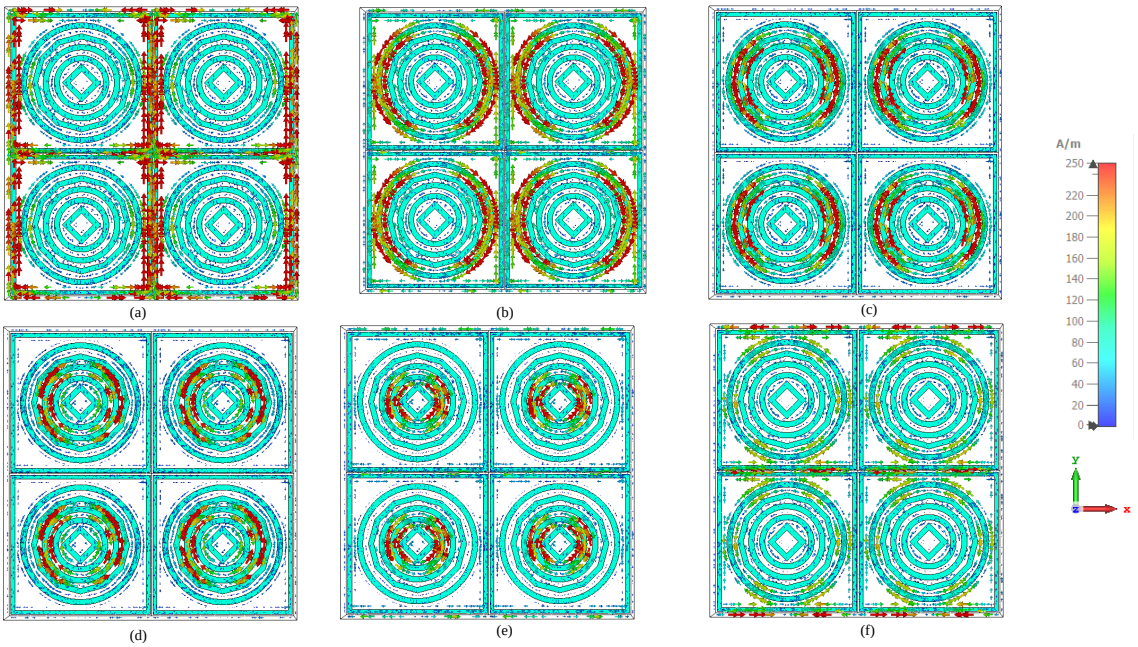

Figure 8. (a)–(f) Surface current responses of the proposed multi band absorber at 2.38, 5.2, 6.8, 9.7, 12.6, and 14.96 GHz, showing the evolution of current concentration across the outer, intermediate, and inner resonant structures.

 doi:10.20944/preprints202604.1889.v1

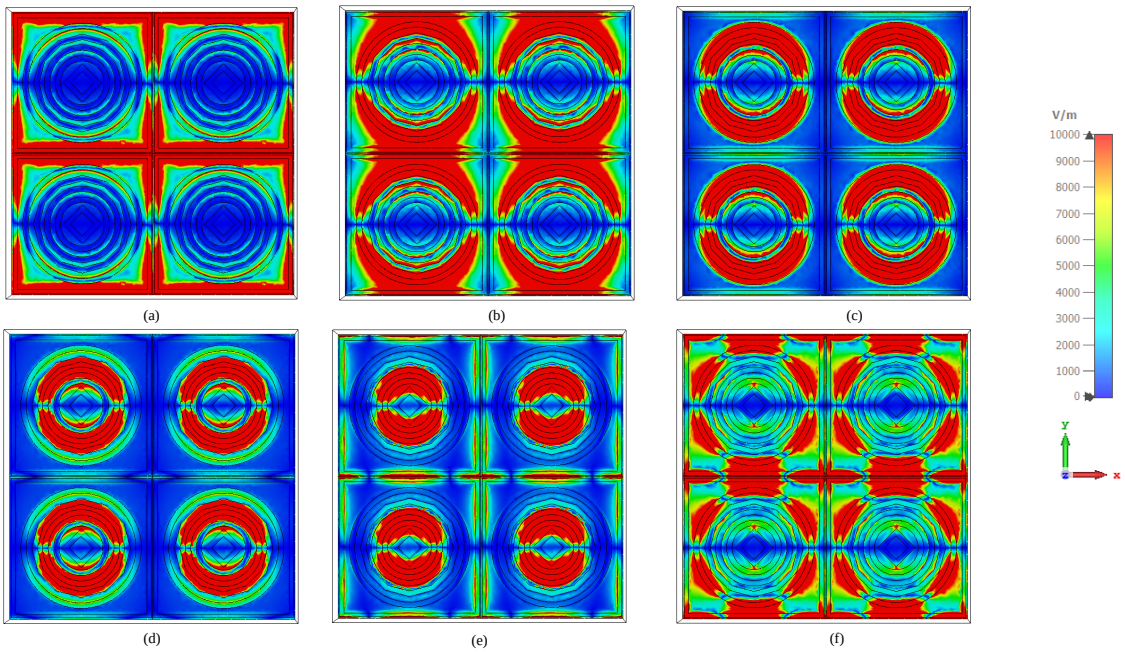

Figure 9. (a)–(f) Electric-field responses of the proposed hexaband absorber at 2.38, 5.2, 6.8, 9.7, 12.6, and 14.96 GHz, showing the evolution of field concentration across the outer, intermediate, and inner resonant structures.

8. The Absorber Is Characterized by Its Frequency-Dependent Permittivity, Permeability, and Impedance

The behavior of the proposed metamaterial absorber (MMA) can be understood through its effective electromagnetic properties, specifically the relative permittivity (ε_r), relative permeability (μ_r), and normalized impedance (Z). These quantities describe the interaction between the structure and the incident electromagnetic field and play a key role in determining its absorption performance. The effective parameters ε_r and μ_r are retrieved from the simulated scattering data using the Nicolson–Ross–Weir (NRW) method, which utilizes the reflection (S_{11}) and transmission (S_{21}) coefficients. This approach is commonly employed to evaluate equivalent material properties from S-parameters. The corresponding relations are given by

$$\varepsilon_r = \frac{c}{j2\pi ft} \cdot \frac{(1 - S_{11}) - S_{21}}{(1 + S_{11}) + S_{21}}, \tag{3}$$

$$\mu_r = \frac{c}{j2\pi ft} \cdot \frac{(1 + S_{11}) - S_{21}}{(1 - S_{11}) + S_{21}}, \tag{4}$$

where c is the speed of light in free space, f denotes frequency, and t corresponds to the substrate thickness. Using these extracted parameters, the normalized impedance of the structure is obtained as

$$Z = \sqrt{\frac{\mu_r}{\varepsilon_r}}. \tag{5}$$

Figures 10–12 shows how ε_r, μ_r, and Z vary with frequency. Near the resonances around 2.38, 5.2, 6.8, 9.7, 12.6, and 14.96 GHz, the real parts of ε_r and μ_r exhibit opposite polarity, indicating strong resonant interaction within the absorber. At the same frequency, the imaginary components increase significantly, reflecting enhanced loss mechanisms that contribute to energy dissipation inside the structure. To further understand the absorption process, impedance matching is considered. When the

 doi:10.20944/preprints202604.1889.v1

input impedance approaches that of free space, reflection is minimized, which is a necessary condition for achieving high absorption . The reflection coefficient can be expressed as

$$S_{11} = \left| \frac{Z/Z_0 - 1}{Z/Z_0 + 1} \right|, \tag{6}$$

where $Z_0 = 377\ \Omega$ represents the intrinsic impedance of free space. At approximately 2.38, 5.2, 6.8, 9.7, 12.6, and 14.96 GHz, the impedance approaches $Z \approx 1 + j0$, indicating near-perfect matching with free space. Under this condition, reflection is significantly reduced, and the incident electromagnetic energy is effectively dissipated within the structure, leading to high absorption performance.

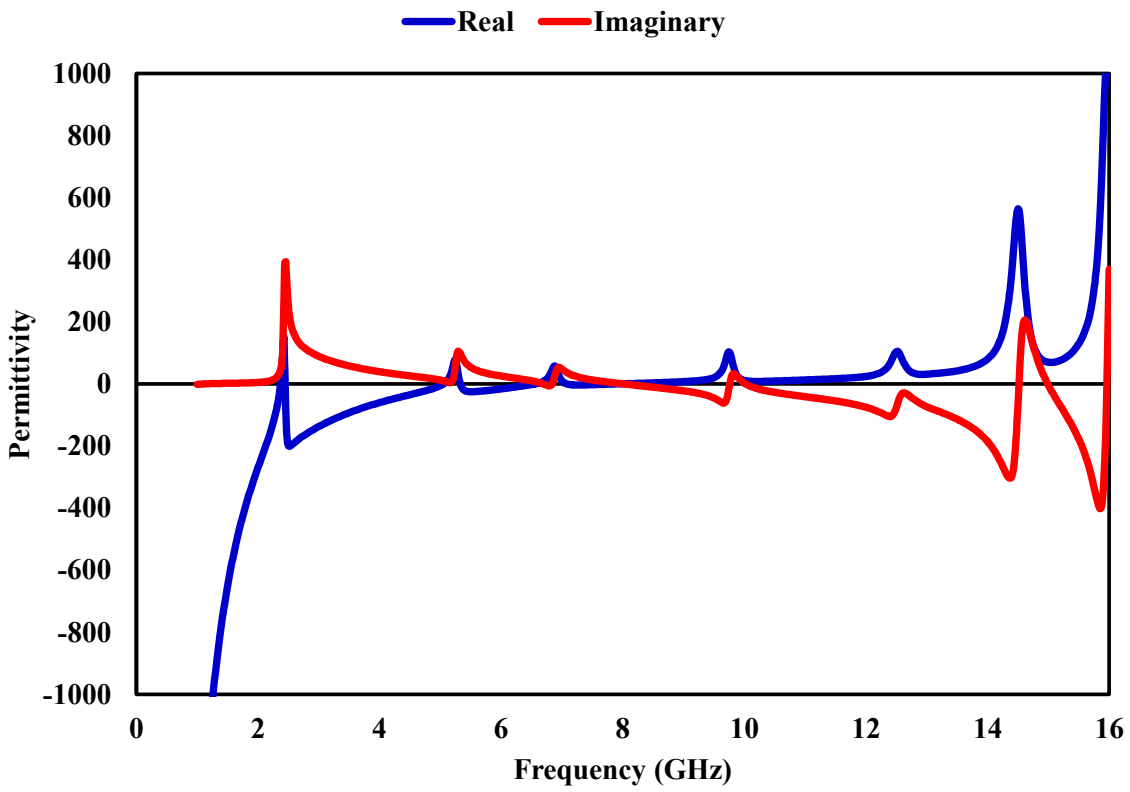

Figure 10. Real and imaginary components of the effective permittivity of the proposed MMA.

 doi:10.20944/preprints202604.1889.v1

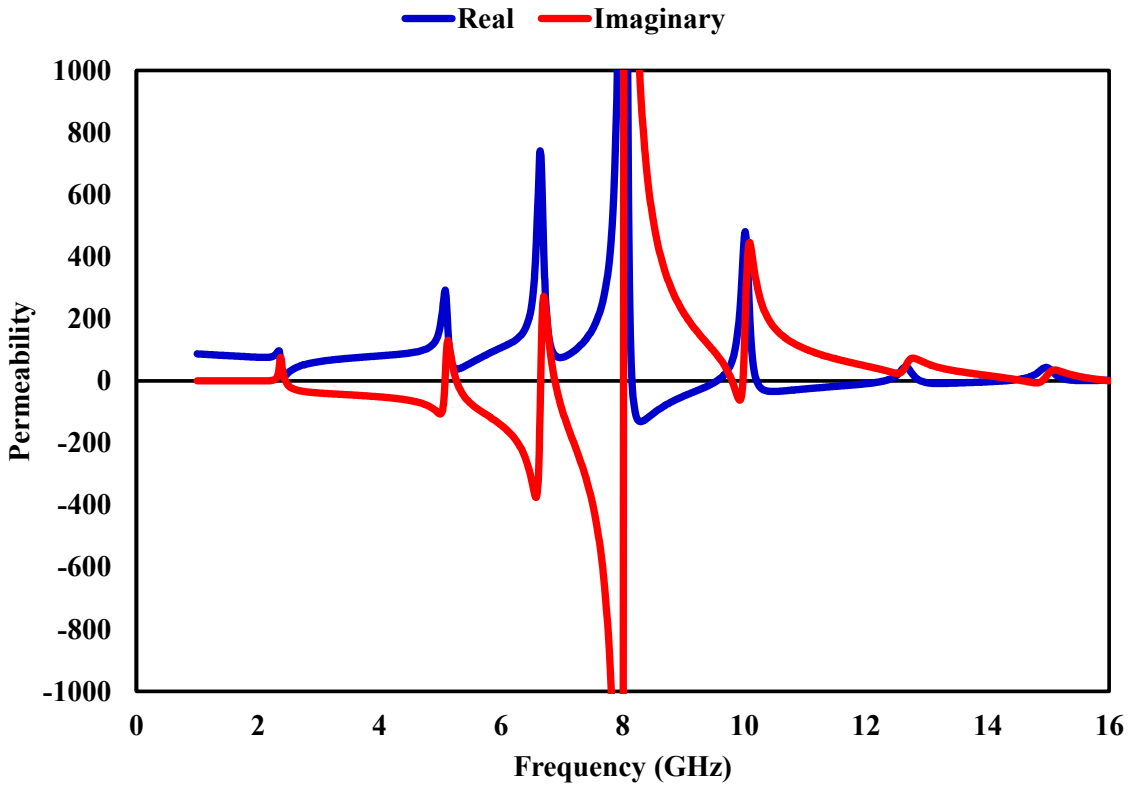

Figure 11. Real and imaginary components of the effective permeability of the proposed MMA.

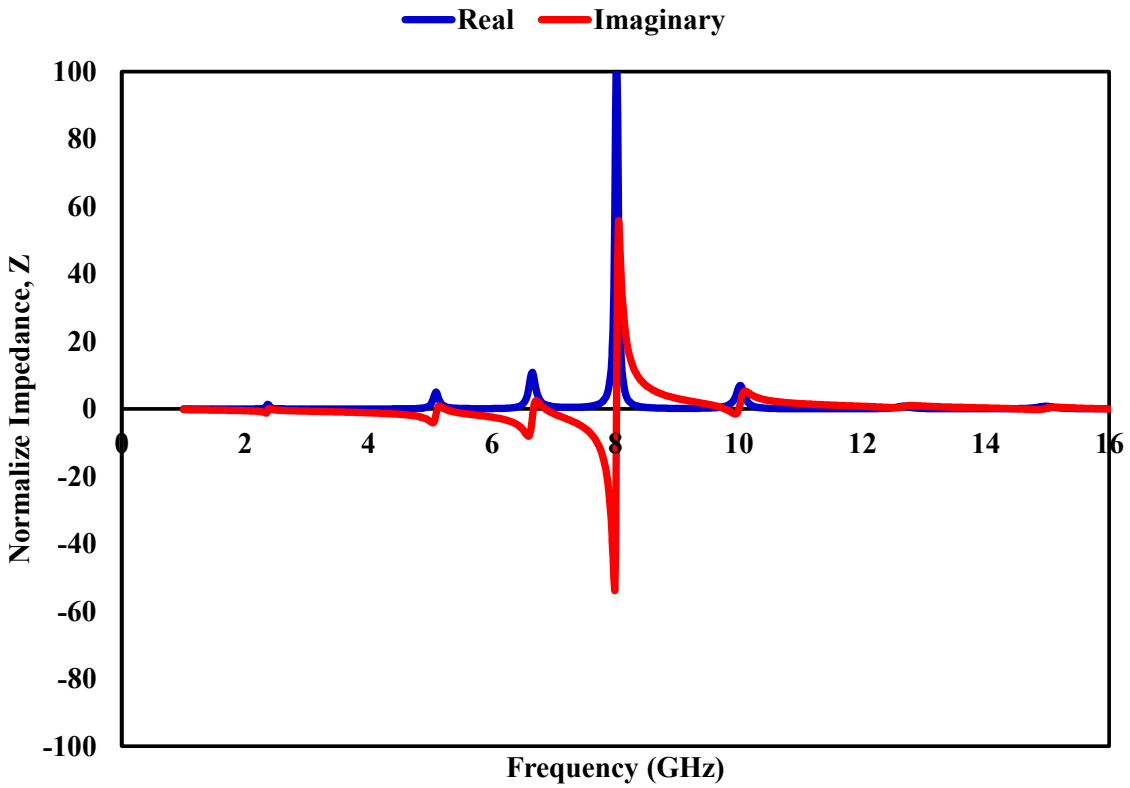

Figure 12. Normalized equivalent impedance response of the hexaband absorber.

 doi:10.20944/preprints202604.1889.v1

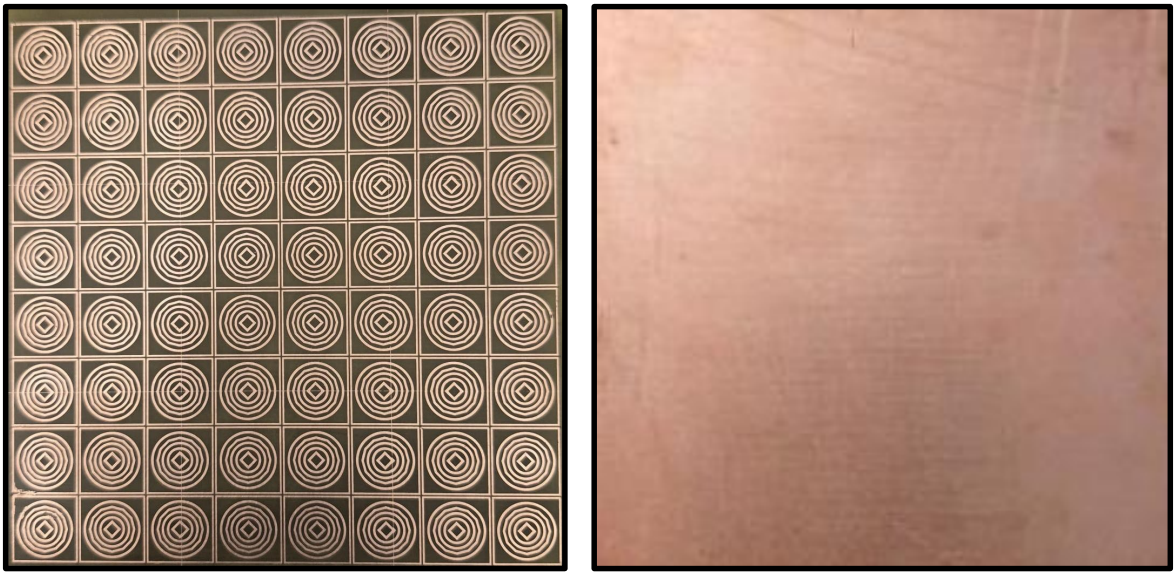

(a) (b)

Figure 13. Fabrication and experimental validation of the proposed structure: (a) front view and (b) back view.

9. Measured Results

To assess the practical performance of the designed metamaterial absorber (MMA), a physical prototype was fabricated and characterized experimentally. An image of the fabricated sample is provided in Figure 14. The prototype is composed of an 8×8 periodic arrangement of unit cells, forming an overall structure with dimensions of 104×104 mm^2. Such an array size is sufficiently large to emulate an effectively infinite surface when illuminated by a plane wave. The experimental investigation was carried out using a free-space measurement configuration, as illustrated in Figure 15. In this setup, a horn antenna connected to a vector network analyzer (VNA) was used to transmit and receive electromagnetic waves. Prior to testing the absorber, a metallic reference plate made of copper was placed at the measurement position to establish a baseline response for calibration. This step ensures that the reflected signal can be properly normalized, which is a standard procedure in free-space measurements After calibration, the fabricated absorber was positioned at the same location under identical measurement conditions, and the corresponding scattering parameters were recorded. The absorption response was then obtained by comparing the measured data of the absorber with the reference signal. Figure 15 presents the comparison between simulated and measured absorption results. The experimental data closely follows the simulated trends over the operating frequency range, confirming the validity of the proposed design. Minor deviations in resonance position and absorption magnitude are present, which can be attributed to fabrication inaccuracies, finite array dimensions, slight positioning errors during measurement, and environmental influences. Overall, the measured results demonstrate that the fabricated absorber maintains its performance in practical conditions, verifying its effectiveness for real-world electromagnetic applications.

 doi:10.20944/preprints202604.1889.v1

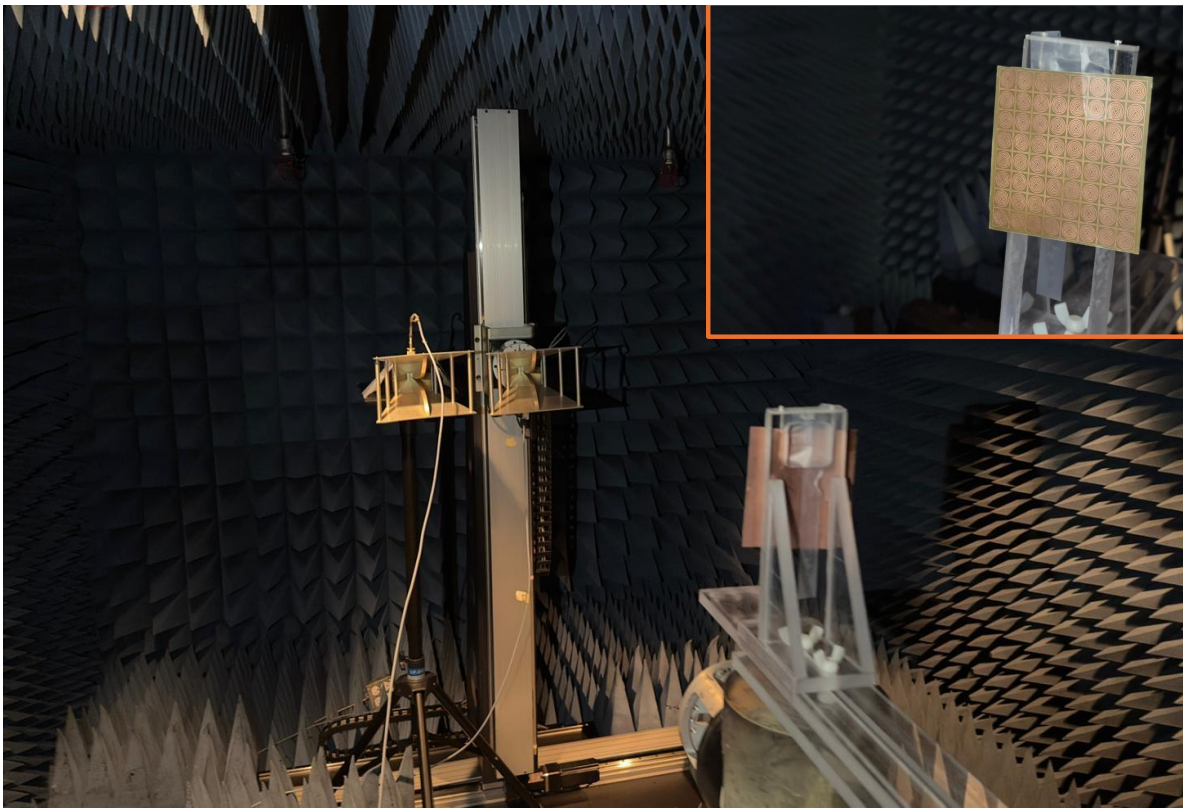

Figure 14. Block diagram representing the practical free-space measurement setup.

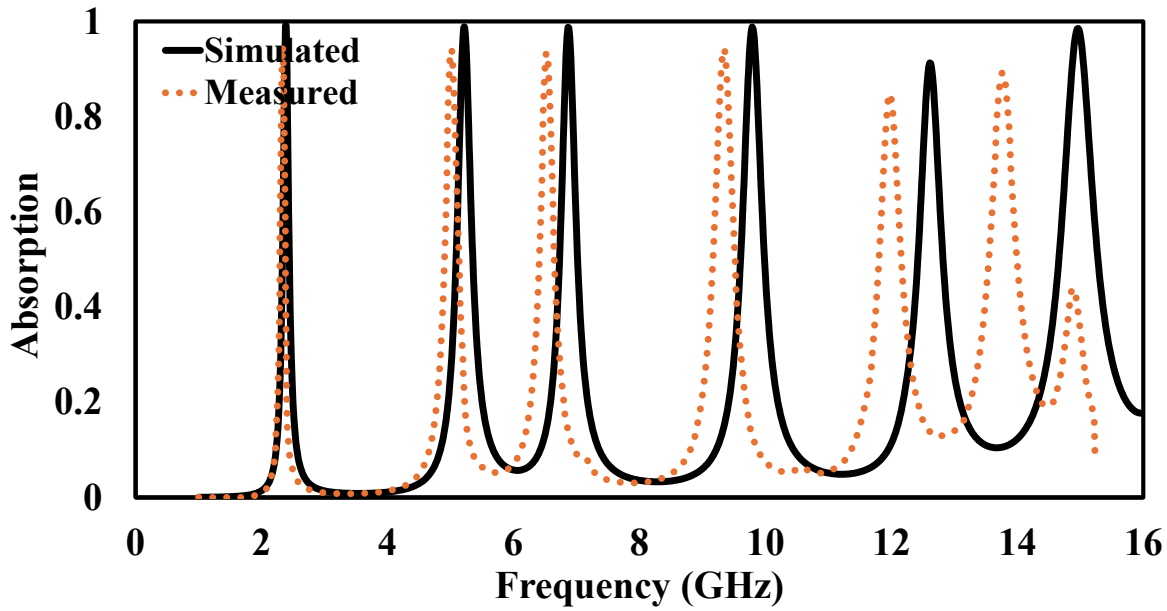

Figure 15. Comparison of simulated and measured absorptivity of the proposed metamaterial absorber.

10. Comparative Study with Previously Published Metamaterial Absorbers

Table 2 presents a comparative evaluation of the proposed metamaterial absorber with previously reported designs in terms of unit-cell size, operating frequency bands, absorption efficiency, polarization insensitivity, and application areas. It can be observed that earlier works demonstrate high absorption performance; however, many are limited either in terms of operating frequency range, polarization dependence, or application diversity. In contrast, the proposed design exhibits a compact unit-cell size of 13×13 mm^2 while supporting multiple resonant frequencies spanning from 2.4 GHz

 doi:10.20944/preprints202604.1889.v1

to 15 GHz. Compared to existing studies, which typically operate over fewer bands or narrower frequency ranges, the proposed absorber achieves a wider multi-band response. Additionally, the absorption levels consistently remain above 97%, indicating superior efficiency across all operating bands. Furthermore, while some reported designs lack polarization-insensitive behavior, the proposed absorber maintains stable performance under different polarization conditions, enhancing its practical applicability. The ability to operate across S-, C-, X-, and Ku-bands further distinguishes the proposed structure from prior works, which are often limited to specific applications such as WLAN, radar, or energy harvesting. Overall, the comparison demonstrates that the proposed MMA offers a favorable balance between compact size, wide frequency coverage, high absorption efficiency, and polarization-independent operation, making it a competitive candidate for advanced electromagnetic and microwave applications.

Table 2. A Comparative Study Between the Proposed Design and Existing Metamaterial Absorbers Benchmarks.

Ref.	Year	UC Size	Freq. (GHz)	Abs. (%)	PI	Application
[38]	2023	20×20	2.4, 3.5, 5.8	99.3, 95.6, 99.5	Yes	WLAN, 5G
[39]	2019	10×10	5.57, 7.97, 13.44	98.9, 97.9, 99.28	Yes	Radar detection
[40]	2019	24×24	8.6, 10.2, 11.95	>80	Yes	Not mentioned
[41]	2022	28.3×28.3	2.4, 5.2, 5.8	99.98	No	Energy harvesting
[42]	2023	17×17	20.38–25.12	97.8–99.3	Yes	5G communication
[43]	2021	10.4×10.4	3.2, 5.32, 11.15, 16.73	95.7–97.7	Yes	S/C/X bands
[44]	2022	8×8	24, 28	98, 94	No	5G communication
[45]	2025	24×24	1.8, 3.5	98.7, 99.7	yes	EMI shielding
Prop	**2026**	**13×13**	**2.4, 5.21, 6.88, 9.77, 12.61, 15**	**98.23, 97.98,98.23, 97.73, 91.13, 97.43**	**Yes**	**S/C/X/ku**

Author Contributions: Conceptualization, I. U. D. and D. K.; Methodology, I. U. D. and D. K.; Software, I. U. D. and D. K.; Validation, I. U. D., D. K., and S. A.; Formal analysis, I. U. D., D. K., and S. A.; Investigation, I. U. D., D. K., and S. A.; Resources, I. U. D. and D. K.; Data curation, I. U. D., D. K., and S. A.; Writing original draft preparation, I. U. D. and D. K.; Writing—review and editing, I. U. D., D. K., S. A., and T. A. D.; Visualization, I. U. D. and D. K.; Supervision, T. A. D.; Project administration, T. A. D.; Funding acquisition, T. A. D. All authors have read and approved the final version of the manuscript.

Funding: The project is funded by Fonds de recherche du Québec Nature et technologies, grant number 370145.

Data Availability Statement: The original contributions presented in this study are included in the article material. Further inquiries can be directed to the corresponding author.

Conflicts of Interest: There are no competing interests to report. The funders had no role in the design of the study; in the collection, analyses, or interpretation of data; in the writing of the manuscript, or in the decision to publish the results.

References

1. Smith, D.R.; Pendry, J.B. Homogenization of metamaterials by field averaging. *Journal of the Optical Society of America B* **2006**, *23*, 391–403.
2. Liu, Y.; Zhang, X. Metamaterials: a new frontier of science and technology. *Chemical Society Reviews* **2011**, *40*, 2494–2507.
3. Costa, F.; Monorchio, A. A frequency selective radome with wideband absorbing properties. *IEEE transactions on antennas and propagation* **2012**, *60*, 2740–2747.
4. Routray, P.; Ghosh, D. Wide-band metamaterial absorber for sub-6 GHz 5G applications: Reducing specific absorption rate. *AEU-International Journal of Electronics and Communications* **2025**, *193*, 155709.
5. Singh, N.; Dhara, R.; Ranjan, S.K. High-performance metamaterial absorber for electromagnetic interference shielding at X-band frequencies. *Optical and Quantum Electronics* **2026**, *58*, 3.
6. Salisbury, W.W. Absorbent body for electromagnetic waves **1952**.
7. Sandiman, S.A.; Dewangan, L.; Tripathi, S.; Dhaliwal, B.S.; Acharjee, J.; Mishra, N.K. HSF-54 resistive ink based screen printed single layered FSS absorber for stealth technology. *Frequenz* **2026**, *80*, 25–38.
8. Luan, J.; Chen, T.; Yang, W.; Zhang, X.; Zhao, X.; Zhao, Y.; He, H. Ultrawideband metamaterial absorber

 doi:10.20944/preprints202604.1889.v1

covering X-and Ku-bands with a single-layer design. *Journal of Electromagnetic Waves and Applications* **2026**, pp. 1–15.
9. Nipun, M.K.; Moniruzzaman, M.; Ahmed, F.S.; Rana, S.R.; Morshed, M.G. From Narrowband to Wideband: A Review of Metamaterial Absorber Design and Development. *IUBAT Review* **2025**, *8*, 145–175.
10. Pendry, J.B.; Holden, A.J.; Robbins, D.J.; Stewart, W.J. Magnetism from conductors and enhanced nonlinear phenomena. *IEEE transactions on microwave theory and techniques* **1999**, *47*, 2075–2084.
11. Shelby, R.A.; Smith, D.R.; Schultz, S. Experimental verification of a negative index of refraction. *science* **2001**, *292*, 77–79.
12. Wu, L.; Yang, L.; Cai, B.; Cheng, Y.; Cheng, Z. Ultra-broadband plasmonic perfect metamaterial absorber based on all-dielectric triple-vertical-ring nanostructure MXene for full-spectrum solar energy. *Physica B: Condensed Matter* **2025**, *708*, 417205.
13. Watts, C.M.; Liu, X.; Padilla, W.J. Metamaterial electromagnetic wave absorbers. *Advanced materials* **2012**, *24*, OP98–OP120.
14. Errajraji, K.; Jebbor, N.; Das, S.; Islam, T.; Madhav, B.T.P.; El-Arrouch, T. Design and analysis of a multi-band miniaturized metamaterial absorber for wireless communication applications. *Optical and Quantum Electronics* **2024**, *56*, 232.
15. Khalil, M.A.; Islam, M.T.; Yong, W.H.; Islam, M.S.; Goh, H.H.; Kurniawan, T.A.; Junejo, N.U.R.; Soliman, M.S.; Khawaja, A.W. Design and validation of a multi-band metamaterial absorber for microwave applications. *AEU-International Journal of Electronics and Communications* **2025**, *193*, 155718.
16. Li, Y.; Wu, Y.; Li, D.; Zhu, M.; Qiu, Y.; Yu, G.; Li, E. A miniaturized perfect metamaterial absorber for EMI radiation suppression. *IEEE Transactions on Electromagnetic Compatibility* **2024**, *66*, 776–786.
17. Uddin, M.K.; Hakim, M.L.; Alam, T.; Islam, M.T.; Alsaif, H.; Islam, M.S. Polarization insensitive eye-shape enclosed split ring resonator-based multi-band metamaterial absorber/sensor for S, C, X, Ku, and K-band microwave applications. *Journal of Sandwich Structures & Materials* **2025**, *27*, 235–259.
18. Hussain, A.; Dong, J.; Abdulkarim, Y.I.; Karim, A.S.; Shi, R. Design, fabrication, and characterization of a broadband metamaterial absorber for Ku-band applications. *Journal of Electronic Materials* **2025**, pp. 1–15.
19. Dong, F.Y.; Niu, C.; Zhang, M.; Wang, A.; Duan, K.; Zhao, J.; Zhu, W.; Hou, Z. A lightweight ultra-wideband metasurface microwave absorber. *Advanced Materials Technologies* **2025**, *10*, 2401493.
20. Alzamil, A.; Khalil, M.A.; Yong, W.H.; Alenezi, A.M.; Alawad, M.A.; Maash, A.A.; Soliman, M.S.; Hussain, R.; Islam, M.T. Design and Performance Evaluation of a Multi-Band Metamaterial Absorber for Oil Quality Sensing. *Journal of Science: Advanced Materials and Devices* **2025**, p. 101081.
21. Elalaouy, O.; Das, S.; El Ghzaoui, M.; Algarni, A.D.; Madhav, B.T.P.; Foshi, J. An ultra-thin polarization-sensitive quad-band metamaterial absorber (QMMA) with Ten absorption peaks for diversified advanced millimeter-wave wireless applications. *Journal of Electronic Materials* **2025**, pp. 1–20.
22. Younis, F.; Khan, O.; Ahmad, J.; Qasim, M.J.; Luo, H.; Wang, S. A highly efficient triple band metasurface enabled absorber for 5G/6G millimeter wave applications. *Scientific Reports* **2025**, *15*, 29455.
23. Luo, Z.; Ji, S.; Zhao, J.; Dai, H.; Jiang, C. Design and analysis of an ultra-thin dual-band wide-angle polarization-insensitive metamaterial absorber for C-band application. *Optik* **2021**, *243*, 166785.
24. Mishra, R.K.; Datar, S. Design, Simulation, and Fabrication of High-Bandwidth Metamaterial Microwave Absorber (MMA) in X-band for EMI Shielding and Stealth Capability. *Journal of Electronic Materials* **2023**, *52*.
25. Zhang, Y.; Dong, H.; Mou, N.; Chen, L.; Li, R.; Zhang, L. High-performance broadband electromagnetic interference shielding optical window based on a metamaterial absorber. *Optics Express* **2020**, *28*, 26836–26849.
26. Saadeldin, A.S.; Sayed, A.M.; Amr, A.M.; Sayed, M.O.; Hameed, M.F.O.; Obayya, S. Broadband polarization insensitive metamaterial absorber. *Optical and Quantum Electronics* **2023**, *55*, 652.
27. Qu, Z.; Hao, J.; Jing, H.; Wei, Y.; Duan, J.; Wang, J.; Zhang, B. An ultra-thin ultra-broadband microwave absorber for radar stealth. *Advanced Composites and Hybrid Materials* **2022**, *5*, 1778–1785.
28. Kumar, A.; Sen, G.; Ghosh, J. Polarization-independent wideband meta-material rasorber with wide transmission window based on resistor loaded circular and split ring resonators. *Advanced Electromagnetics* **2025**, *14*.
29. Zhou, Z.; Chen, K.; Zhu, B.; Zhao, J.; Feng, Y.; Li, Y. Ultra-wideband microwave absorption by design and optimization of metasurface salisbury screen. *IEEE Access* **2018**, *6*, 26843–26853.
30. Weng, Z.; Li, Y.; Su, Y.; Li, Z.; Guo, J.; Lv, Z.; Liang, C. Design and Analysis of Ultra-Thin Broadband Transparent Absorber Based on ITO Film. *Micromachines* **2025**, *16*, 653.
31. Matei, A.T.; Vișan, A.I.; Popescu-Pelin, G.F. Design and processing of metamaterials. *Crystals* **2025**, *15*, 374.

 doi:10.20944/preprints202604.1889.v1

32. Zhang, S.; Zheng, J.; Zhao, Z.; Du, S.; Lan, D.; Gao, Z.; Wu, G. New prospects in built-in electric fields for electromagnetic wave absorption: from fundamentals to interdisciplinary applications. *Advanced Functional Materials* **2025**, p. e13762.
33. Wang, Y.; Zhang, X.; Wang, Y.; Liu, Y.; Li, J.; Chen, X.; Cui, Z.; Burokur, S.N.; Zhang, J.; Zhao, X.; et al. Recent advances in metasurfaces: from THz biosensing to microwave wireless communications. *Research* **2025**, *8*, 0820.
34. Cheng, Y.Z.; Cheng, Z.Z.; Mao, X.S.; Gong, R.Z. Ultra-thin multi-band polarization-insensitive microwave metamaterial absorber based on multiple-order responses using a single resonator structure. *Materials* **2017**, *10*, 1241.
35. Wakatsuchi, H.; Kim, S.; Rushton, J.J.; Sievenpiper, D.F. Circuit-based nonlinear metasurface absorbers for high power surface currents. *Applied Physics Letters* **2013**, *102*.
36. Yoo, M.; Lim, S. Polarization-independent and ultrawideband metamaterial absorber using a hexagonal artificial impedance surface and a resistor-capacitor layer. *IEEE transactions on antennas and propagation* **2014**, *62*, 2652–2658.
37. Ghosh, S.; Srivastava, K.V. An equivalent circuit model of FSS-based metamaterial absorber using coupled line theory. *IEEE Antennas and Wireless Propagation Letters* **2014**, *14*, 511–514.
38. Rahman, A.A.M.; Islam, M.T.; Moniruzzaman, M.; Misran, N.; Alorifi, F.; Shamsan, Z.A.; Almuhanna, K.; Rahim, S.K.A.; Islam, M.S.; Soliman, M.S. Triple band frequency tunable polarization insensitive metamaterial absorber for WLAN and 5G applications. *Optical Materials* **2023**, *145*, 114368.
39. Dhillon, A.S.; Mittal, D.; Bargota, R. Triple band ultrathin polarization insensitive metamaterial absorber for defense, explosive detection and airborne radar applications. *Microwave and optical technology letters* **2019**, *61*, 89–95.
40. Jafari, F.S.; Naderi, M.; Hatami, A.; Zarrabi, F.B. Microwave Jerusalem cross absorber by metamaterial split ring resonator load to obtain polarization independence with triple band application. *AEU-International Journal of Electronics and Communications* **2019**, *101*, 138–144.
41. Wei, Y.; Duan, J.; Jing, H.; Lyu, Z.; Hao, J.; Qu, Z.; Wang, J.; Zhang, B. A multiband, polarization-controlled metasurface absorber for electromagnetic energy harvesting and wireless power transfer. *IEEE Transactions on Microwave Theory and Techniques* **2022**, *70*, 2861–2871.
42. Mohammed, S.A.; Albadri, R.A.K.; Al-Badri, K.S.L. Simulation of the microwave five-band perfect metamaterial absorber for 5G communication. *Heliyon* **2023**, *9*.
43. Singh, R.K.; Gupta, A. A wrenched-square shaped polarization independent and wide angle stable ultra-thin metamaterial absorber for S-band, X-band and Ku-band applications. *AEU-International Journal of Electronics and Communications* **2021**, *132*, 153648.
44. Naqvi, S.A.; Baqir, M.A.; Gourley, G.; Iftikhar, A.; Saeed Khan, M.; Anagnostou, D.E. A novel meander line metamaterial absorber operating at 24 GHz and 28 GHz for the 5G applications. *Sensors* **2022**, *22*, 3764.
45. Moniruzzaman, M.; Larguech, S.; Mobarak, M.; Jizat, N.M.; Alharbi, S.S.; Islam, M.T.; Samsuzzaman, M.; Al-Bawri, S.S. Dual band polarization insensitive metamaterial absorber for EMI shielding from GSM and 5G communication systems. *Scientific Reports* **2025**, *15*, 12292.